Editors' Suggestion | Featured in Physics

Deterministic Single-Ion Implantation of Rare-Earth Ions for Nanometer-Resolution Color-Center Generation

Karin Groot-Berning,[1,†] Thomas Kornher,[2] Georg Jacob,[1,*] Felix Stopp,[1] Samuel T. Dawkins,[3] Roman Kolesov,[2] Jörg Wrachtrup,[2] Kilian Singer,[3] and Ferdinand Schmidt-Kaler[1]

[1]*QUANTUM, Institut für Physik, Universität Mainz, Staudingerweg 7, 55128 Mainz, Germany*

[2]*Physikalisches Institut, Universität Stuttgart, 70569 Stuttgart, Germany*

[3]*Experimentalphysik I, Institut für Physik, Universität Kassel, Heinrich-Plett-Straße 40, 34132 Kassel, Germany*

(Received 28 March 2019; published 4 September 2019)

Single dopant atoms or dopant-related defect centers in a solid state matrix are of particular importance among the physical systems proposed for quantum computing and communication, due to their potential to realize a scalable architecture compatible with electronic and photonic integrated circuits. Here, using a deterministic source of single laser-cooled Pr^+ ions, we present the fabrication of arrays of praseodymium color centers in yttrium-aluminum-garnet substrates. The beam of single Pr^+ ions is extracted from a Paul trap and focused down to 30(9) nm. Using a confocal microscope, we determine a conversion yield into active color centers of up to 50% and realize a placement precision of 34 nm.

DOI: 10.1103/PhysRevLett.123.106802

Deterministic doping methods at the nanometer scale provide a route towards scalable quantum information processing in solid state systems. Prominent examples of atomic systems in solid state hosts for quantum computing are single phosphorus atoms in silicon [1] and spin-correlated pairs of such donors [2,3], which have led to studies of the scalability of large arrays of coupled donors [4]. Alternatively, single color centers [5] and the growing variety of single rare-earth ions (REIs) doped into crystalline hosts are studied for likewise reasons [6–15]. Driven by proposed quantum applications, the need to deterministically place single dopants into nanostructured devices has led to the development of various techniques related to the silicon material system [16,17]. Crystalline hosts of color centers and REIs, however, typically exhibit poor electronic properties, which inhibits single-ion detection via active substrates [16], and therefore an alternative technique for deterministic implantation of dopants is required. Here, we present an inherently deterministic method for single-ion implantation based on a segmented Paul trap which allows for implantation in any solid state material with a broad range of implantation energies.

For characterizing the implantation method, we use single praseodymium ion detection in yttrium-aluminum-garnet (YAG) crystals based on up-conversion microscopy. This detection scheme requires implanted praseodymium ions to arrange in the proper lattice position and reach the Pr^{3+} charge state through a suitable annealing and activation procedure. An accurate determination of the ratio of detected ions to implanted ions, commonly referred to as the implantation yield, has been performed for the first time at the level of single ions and will further foster the optimization of annealing procedures. In comparison to previous implantation-based nitrogen and silicon vacancy color-center generation experiments [18], we achieve a more than 20 times higher yield for the implantation of Pr^+ in YAG, even at much lower implantation energies with correspondingly smaller straggling-related uncertainty of the implantation site.

This Letter is organized as follows: After introducing the apparatus and procedures for deterministic implantation, we characterize the Pr^{3+} centers in YAG samples through confocal two-photon microscopy imaging. We discuss the spatial uncertainty of both single and arrays of REI-generated color centers, also sketching further plans for applications and improvements. At the heart of the experimental apparatus is an ion trap, which acts as a source of single $^{141}Pr^+$ ions. The source is realized by loading the ions into the trap, where they are cooled, identified, and subsequently extracted towards the implantation section [see Fig. 1(a)]. The ion trap consists of two segmented dc and rf electrodes in an X-shaped configuration with two end cap electrodes at a distance of 2.9 mm [19]. We operate the trap with a radio frequency of $\Omega_{\mathrm{rf}} = 2\pi \times 23.062$ MHz at a peak-to-peak amplitude of $V_{\mathrm{pp}} = 572$ V, which leads to $\omega_{\mathrm{ax,r1,r2}} = 2\pi \times \{0.45, 1.584, 1.778\}$ MHz for the axial and radial mode frequencies of a single $^{40}Ca^+$ ion. We load mixed crystals of $^{141}Pr^+$ and $^{40}Ca^+$ ions and employ laser cooling on the $S_{1/2}$ to $P_{1/2}$ transition of Ca^+ to sympathetically cool the Pr^+ ions (for details, see Methods Sec. M1 [20]). By imaging the fluorescence of the calcium ions on a camera, we determine the number of trapped ions. The increase of the distance between two bright calcium ions provides evidence for a single praseodymium ion

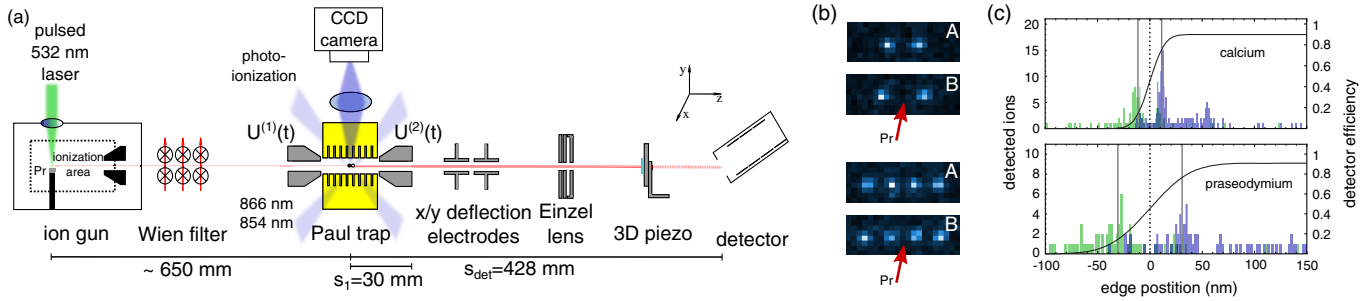

FIG. 1. (a) Sketch of the single-ion implantation setup. (b) Fluorescence of ions imaged. (*A*) Pure Ca^+ crystals; the distance between two Ca^+ ions is 9.5 μm. (*B*) Crystals containing an additional Pr^+ ion. (c) Histograms of the profiling edge measurement for $^{40}Ca^+$ and $^{141}Pr^+$ ions. For calcium, the extraction took about 15 min for 308 ions, whereas for praseodymium it took about 2 h for 150 ions. The events of the single-ion extraction are split into two cases; blue presents the detected ions and green the blocked ions. The black line shows the Bayesian fit function which corresponds to the last measured parameter values for beam position x_0, radius σ, and detector efficiency a. The mean value of the beam position of the x axis is set to $x_0 = 0$ (dotted line), and the gray lines show the 1σ radius of the beam waist, which is $\sigma_{Ca} = 11.3 \pm 2.0$ nm for calcium and $\sigma_{Pr} = 30.7 \pm 8.5$ nm for praseodymium.

trapped between them [see Fig. 1(b)]. We reduce the ion number to exactly one $^{40}Ca^+$ and one $^{141}Pr^+$ by a predefined voltage sequence of the axial trap potential. The ions are extracted with an energy of 5.9 keV. The extraction path is steered by deflection electrodes to the center of an electrostatic einzel lens, which focuses the ions to a small spot. A three-axis piezoelectric translation stage in the focal plane is used to determine the spot size with a profiling edge by moving it into the beam and recording the number of transmitted ions. We employ a Bayesian experimental design method [19] to optimize the chosen profiling edge positions. The spot size measurement for calcium and praseodymium is shown in Fig. 1(c). The measured radius of the beam waist for calcium is $\sigma_{Ca} = 11.3 \pm 2.0$ nm and $\sigma_{Pr} = 30.7 \pm 8.5$ nm in the case of praseodymium (for details, see Secs. M2–M4 [20]). For the case of Doppler-cooled Ca^+ ions with a measured wave packet size of about 52 nm, we found that the spot size is dominated by mechanical vibrations [19]. To understand the spot measurements for Pr^+, however, we conjecture an elevated phonon number of radial modes, corresponding to an increased motional wave packet size, because the sympathetic cooling rate is significantly reduced for differences in the mass-to-charge ratio as high as $141/40 \simeq 3.52$ [21]. Also on the three-axis piezoelectric stage is a YAG crystal, which is moved into the focal plane for implantation. We implanted two dot-grid patterns of praseodymium ions, each with 12 spots with exactly eight (area *A*) and exactly four (area *B*) Pr^+ ions per spot, respectively. The dot-grid spacing was 2 μm, and the implantation energy of 5.9 keV corresponds to an implantation depth of ~6 nm [22]. After implantation, the sample was annealed in air at 1200 °C for approximately 1 min.

Verification of successful color-center generation was demonstrated by the optical detection of trivalent praseodymium ions on the single-ion level [6]. The method is based on a two-photon up-conversion [23], which enhances the efficiency of the excitation-emission cycle and maximizes the fluorescence emission. The electronic level structure of Pr^{3+} ion in the YAG crystal [24] allows for several two-photon excitation schemes [see Fig. 2(a)]. We employ a laser near 487 nm driving a parity-forbidden, and thus spectrally narrow, $4f - 4f$ transition from a $^3H_4$ ground state to a $^3P_0$ shelving state with a lifetime of 8 μs. From the $^3P_0$ state, a second excitation step at 487 nm promotes the electron to the $4f5d$ level via a parity-allowed optical transition. The lowest $4f5d$ level yields emission in a spectral range between 300 and 450 nm [23], with close to unity quantum efficiency [25] and a lifetime of about 18 ns. Such two-photon up-conversion microscopy has the advantage of virtually background-free imaging and was realized by an up-conversion microscope

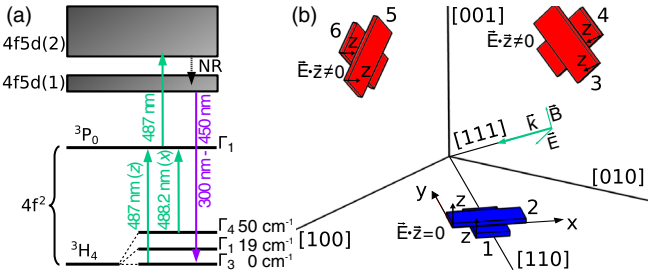

FIG. 2. (a) Electronic level structure of Pr^{3+} in a YAG crystal. For optical characterization, the blue transition (487 nm) originating from Γ_3 and exciting the z dipole directions was used. Levels have symmetry representations Γ_3 (0 cm^{-1}), Γ_1 (19 cm^{-1}), and Γ_4 (50 cm^{-1}). Transitions from a $^3H_4$ to a $^3P_0$ state (Γ_1 symmetry) are polarized either along the z axis or along the x axis. (b) Orientation of the six dodecahedral rare-earth sites, indicated by matchboxes [26]. The excitation laser propagates along the [111], and its polarization is adjusted so that two out of six sites are rendered dark. As an example, sites 1 and 2 are not excited, which leads to sites 3–6 being excited with equal, nonzero probability.

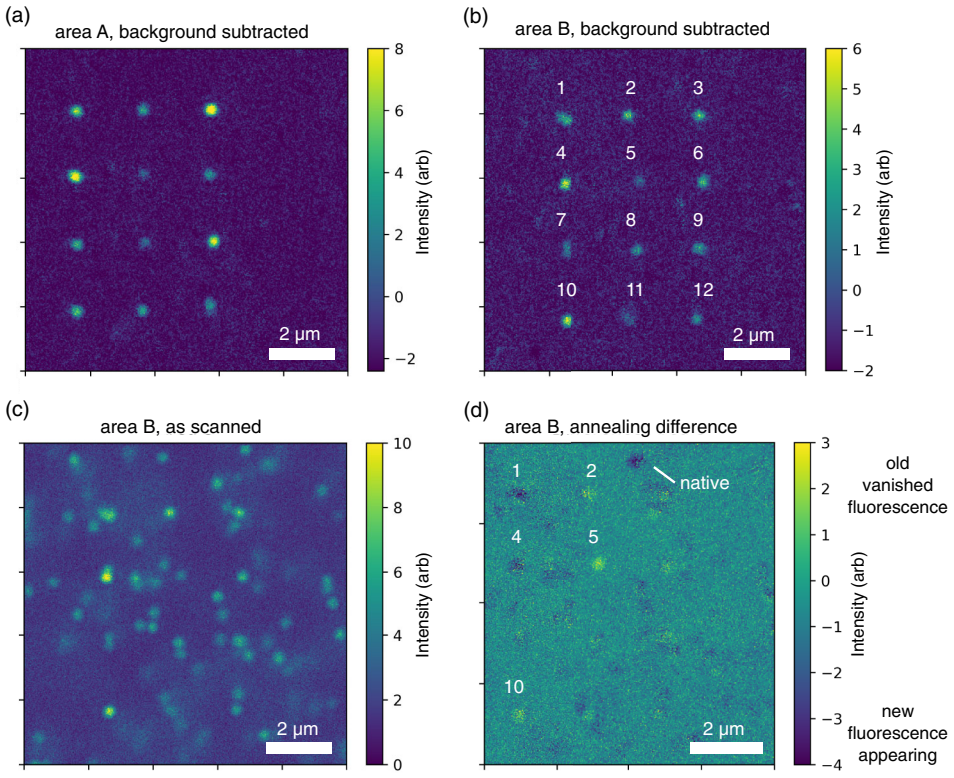

FIG. 3. Up-converting microscopy scans of (a) area A, after subtraction of the preimplantation scanned background. (b) Area B, after subtraction of the preimplantation scanned background. (c) Area B, after the implantation and annealing procedure. (d) Difference in REI fluorescence signals $\Delta C = C_{\text{before}} - C_{\text{after}}$, before and after a second annealing process.

shown schematically in Supplemental Material [20]. Its optical resolution was determined to be 115(3) nm, from the average width of a 2D-Gaussian fit of single Pr^{3+} ion fluorescence. The imaging quality is limited by background fluorescence from other Pr^{3+} impurities, naturally found in the crystal within 1–2 μm below the surface, as shown in Fig. 3(c). We determine a background density of Pr^{3+} ions of 6×10^{11} cm^{-3} or 0.04 ppb relative to yttrium.

Pr^{3+} ions doped into YAG substitute for Y^{3+}. The crystal features six magnetically inequivalent orientations of these particular sites of D_2 symmetry, where the local x, y, and z axes of the Pr^{3+} ion correspond to the [110], [1$\bar{1}$0], and [001] crystal axes and their six equivalent directions [see Fig. 2(b)] [27]. The $^3H_4$ ground state of Pr^{3+} in the crystal field is split into nine levels, of which the lowest three in energy are populated at room temperature. In order to quantify single-ion implantation, we render all detected Pr^{3+} ions equal with respect to the collected fluorescence signal. The linear polarization of the excitation light near 487 nm is switched to all three different polarization orientations, such that two out of six Pr^{3+} sites appear dark, while four states yield equal fluorescence; see Fig. 2(b). This allows for extracting the number of ions residing within the optically resolved spot. Figure 3(c) shows an image of fluorescence of area B, comprising 12 spots each implanted with four praseodymium ions (spot no. 12 of area B has two implanted ions). However, here the implantation pattern neither is clearly visible nor allows for a quantitative analysis on this scanned map, because implanted and preexisting native Pr^{3+} are indistinguishable. Therefore, a background fluorescence image was scanned prior to the Pr^{+} ion implantation, in a designated field of implantation. After implantation, annealing, and imaging, a background subtraction shows the newly generated Pr^{3+} sites; see Fig. 3(b). The same procedure was used to image generated REI sites in a second YAG area A; see Fig. 3(a).

In order to study the effect of the annealing procedure on the REI fluorescence of both native and implanted Pr^{3+} ions, the implanted areas were imaged again after a second annealing step. The difference image is shown in Fig. 3(d), taken on area B. Changes due to the second annealing process are visible, typically at the implantation sites, and are marked by a number. In spots two, five, and ten, respectively, the fluorescence of a single Pr^{3+} ion vanished, while, in spots one and four, exactly one additional Pr^{3+} ion appeared. Only one single native Pr^{3+} ion appeared on a 100 μm^2 area, leading to the conclusion that the annealing procedure has only a marginal effect on the native Pr^{3+} background and our background correction is a valid procedure. We conjecture that the diffusion rate of 2×10^{-21} m^2/s at a temperature of $\sim$1200 °C is responsible

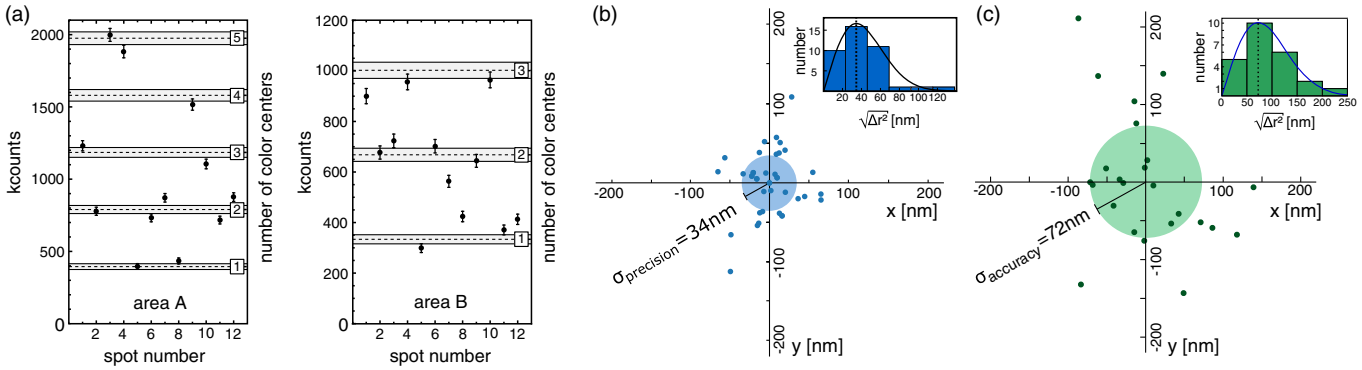

FIG. 4. (a) Net fluorescence signal (per 6 ms and after subtraction of the background) of implanted spots for areas A and B. The observed count rate is consistent with the discrete nature of the integer number of REI emitters per spot. For the error bars, we assume a Poissonian photon-counting statistics. (b) Fitted Pr^{3+} ion locations with respect to the centroid of each respective spot. For this analysis, we excluded the implantation spots 1, 7, and 9 in area B and spot 12 in area A, since these suffer from drifts far larger than the standard deviation of the rest of the implanted spots. The mode of the precision $\sigma_{\text{precision}} = 34$ nm was revealed using the Rayleigh distribution and is an indication of the precision of ion placement. The inset shows the histogram of the radial distances of implanted ions to their center of mass together with the Rayleigh distribution of the data using the maximum likelihood method (black curve) and the mode of the precision $\sigma_{\text{precision}}$ (dotted line). The precision error of the multi-Gaussian fitting method was estimated from Monte Carlo simulations to ± 18 nm. (c) Calculated difference in position between the implanted spots and the ideal grid positions. The mode of the accuracy $\sigma_{\text{accuracy}} = 72$ nm was revealed using the Rayleigh distribution and is an indication of the accuracy of ion placement. The inset shows the histogram of the radial distance from the implantation to the ideal grid position together with the Rayleigh distribution (blue curve) of the data and the mode of the accuracy σ_{accuracy} (dotted line).

for this effect [28]. For shallow locations, 6 nm below the surface, Pr^{3+} ions may diffuse and stabilize at the surface in a nonfluorescing charge state. Shorter annealing times may help to reduce this effect but were not available for our experiments. The enhanced mobility of Pr^{3+} ions in implanted spots as compared to native Pr^{3+} is likely caused by local crystal damage in these sites that occurs even at a low implantation energy of 5.9 keV and single-ion fluence.

Summing up the collected REI fluorescence per spot, after background subtraction, we find approximately integer multiples of single Pr^{3+} ion counts; see Fig. 4(a). Accordingly, each spot is assigned an integer number of optically active Pr^{3+} ions (for details, see [20]). The associated implantation yields are 32% and 50(5)% for area A and area B, respectively. We account only for systematic errors, estimated from the observed annealing-induced ion migration in area B. We conjecture that the lower yield in area A may be attributed to the twice higher implantation dose as compared to area B and thus, a higher probability of lattice defects which have not been fully annealed.

We study the spatial quality of placing REI in the spots: Fitting 2D Gaussian profiles onto native single Pr^{3+} fluorescence images reveals an optical circular single-ion point spread function (PSF) of the confocal microscope of 115 nm. Setting this width, we fit each of the implanted spots with a multi-Gaussian, according to the number of REIs in that spot. The extracted positions of fitted PSFs are displayed relative to the center of mass of the respective spot in Fig. 4(b). The mode of the radial distance, the value that is most likely, is $\sigma_{\text{precision}} = 34$ nm and indicates a measure of the position stability. Note that the Pr^{+} ion beam size of about 30 nm dominates the position stability, while straggling uncertainties and annealing-induced migration can further add to this value. A Monte Carlo simulation of the multi-Gaussian fitting method was used to estimate the precision error of ± 18 nm [20]. The deviation of implantation spots off the desired grid is characterized as a patterning accuracy. For this, we extract the center of each fluorescent spot from a 2D-Gaussian fit (independent of the number of color centers in the spot) and calculate its difference to an ideal grid with exactly 2 μm spacing. The derivation is characterized by the mode of the distribution with a value of $\sigma_{\text{accuracy}} = 72$ nm, was determined from a Rayleigh distribution using the maximum likelihood method, and characterizes the accuracy for array writing; see Fig. 4(c). The main contribution to the uncertainty comes from nonlinearities of the piezoelectric translation stage, which causes according to manufacturer specifications distortions of about 40 nm to the desired dot-grid spacing. We note that the accuracy of placement in the x direction in area B was noticeably worse than the other direction, which we conjecture is due to long-term thermal drifts.

In conclusion, we have demonstrated deterministic ion implantation and the writing of an array of Pr^{3+} ions in YAG. The characterization of implantation sites by two-photon confocal microscopy shows a yield of Pr^{3+} ions in YAG of up to 50%. Improving the annealing procedures could allow for approaching 100% and thus deterministic

generation of REI dopants in crystals. Note that the single-ion implantation technique may be applied for a large range of materials, doping ions, and implantation energies, which gives rise to new options for fabricating quantum devices, such as arrays of phosphorus qubits in an ultrapure silicon crystal. We demonstrated a 72 nm positioning accuracy, which is adequate for generating photonic structures with efficient coupling [29]. The coupling of single implanted spins with superconducting circuits [30] or a direct coupling of ^{31}P nuclear spin qubits at about 15 nm distance according to the Kane proposal [31] will require about an order of magnitude improvement in positioning accuracy. However, the achieved accuracy is already sufficient for implanting arrays of qubits sites at 100–500 nm separation for a recently proposed ^{31}P in a silicon flip-flop qubit, based on electron nuclear spin states [32]. Note that technical reasons such as the piezoelectric translation stage and thermal drifts are dominating present accuracy.

Improving sympathetic cooling of the Pr^{+} ions prior to extraction, as well as increasing the mechanical and thermal stability of the apparatus, we anticipate improving the positioning accuracy to a few nanometers, a regime which is dominated by the implantation-induced straggling. Using superresolution microscopy, which is available in the case of Ce^{3+} ions in YAG [33], a more precise characterization of the implantation systems can be implemented.

F. S.-K. acknowledges financial support by the DFG DIP program (FO 703/2-1) and the Australian Research council within the CQC2T. F. S.-K. and K. S. acknowledge financial support by the VW Stiftung. K. S. and S. T. D. acknowledge financial support from LOEWE (SMolBits). R. K. acknowledges financial support by DFG (Grant No. KO4999/3-1), and R. K. and J. W. acknowledge financial support by the EU via SMeL and QIA as well as the DFG via FOR 2724. The research leading to these results has received funding from the European Union's Horizon 2020 research and innovation program under Grant Agreement No. 820391 (SQUARE).

K. G.-B. and T. K. contributed equally to this letter.

*Present address: Alpine Quantum Technologies GmbH, c/o Greiter Pegger Kofler and Partner, Maria-Theresien-Straße 24, 6020 Innsbruck, Austria.

†karin.groot-berning@uni-mainz.de

[1] M. Koch, J. Keizer, P. Pakkiam, D. Keith, M. House, E. Peretz, and M. Simmons, Nat. Nanotechnol. **14**, 137 (2019).

[2] M. Veldhorst, C. Yang, J. Hwang, W. Huang, J. Dehollain, J. Muhonen, S. Simmons, A. Laucht, F. Hudson, K. Itoh *et al.*, Nature (London) **526**, 410 (2015).

[3] M. Broome, S. Gorman, M. House, S. Hile, J. Keizer, D. Keith, C. Hill, T. Watson, W. Baker, L. Hollenberg *et al.*, Nat. Commun. **9**, 980 (2018).

[4] J. J. Pla, K. Y. Tan, J. P. Dehollain, W. H. Lim, J. J. Morton, D. N. Jamieson, A. S. Dzurak, and A. Morello, Nature (London) **489**, 541 (2012).

[5] A. Gruber, A. Dräbenstedt, C. Tietz, L. Fleury, J. Wrachtrup, and C. v. Borczyskowski, Science **276**, 2012 (1997).

[6] R. Kolesov, K. Xia, R. Reuter, R. Stöhr, A. Zappe, J. Meijer, P. Hemmer, and J. Wrachtrup, Nat. Commun. **3**, 1029 (2012).

[7] A. M. Dibos, M. Raha, C. M. Phenicie, and J. D. Thompson, Phys. Rev. Lett. **120**, 243601 (2018).

[8] T. Zhong, J. M. Kindem, J. G. Bartholomew, J. Rochman, I. Craiciu, V. Verma, S. W. Nam, F. Marsili, M. D. Shaw, A. D. Beyer *et al.*, Phys. Rev. Lett. **121**, 183603 (2018).

[9] T. Kornher, K. Xia, R. Kolesov, B. Villa, S. Lasse, C. S. Sandu, E. Wagner, S. Harada, G. Benvenuti, H.-W. Becker *et al.*, ACS Photonics **4**, 1101 (2017).

[10] S. Marzban, J. G. Bartholomew, S. Madden, K. Vu, and M. J. Sellars, Phys. Rev. Lett. **115**, 013601 (2015).

[11] D. Englund, B. Shields, K. Rivoire, F. Hatami, J. Vuckovic, H. Park, and M. D. Lukin, Nano Lett. **10**, 3922 (2010).

[12] M.-A. Lemonde, S. Meesala, A. Sipahigil, M. J. A. Schuetz, M. D. Lukin, M. Loncar, and P. Rabl, Phys. Rev. Lett. **120**, 213603 (2018).

[13] R. Kolesov, K. Xia, R. Reuter, M. Jamali, R. Stöhr, T. Inal, P. Siyushev, and J. Wrachtrup, Phys. Rev. Lett. **111**, 120502 (2013).

[14] C. Yin, M. Rancic, G. G. de Boo, N. Stavrias, J. C. McCallum, M. J. Sellars, and S. Rogge, Nature (London) **497**, 91 (2013).

[15] T. Utikal, E. Eichhammer, L. Petersen, A. Renn, S. Götzinger, and V. Sandoghdar, Nat. Commun. **5**, 3627 (2014).

[16] J. van Donkelaar, C. Yang, A. D. C. Alves, J. C. McCallum, C. Hougaard, B. C. Johnson, F. E. Hudson, A. S. Dzurak, A. Morello, D. Spemann *et al.*, J. Phys. Condens. Matter **27**, 154204 (2015).

[17] F. J. Rueß, W. Pok, T. C. Reusch, M. J. Butcher, K. E. J. Goh, L. Oberbeck, G. Scappucci, A. R. Hamilton, and M. Y. Simmons, Small **3**, 563 (2007).

[18] T. Schröder, M. E. Trusheim, M. Walsh, L. Li, J. Zheng, M. Schukraft, A. Sipahigil, R. E. Evans, D. D. Sukachev, C. T. Nguyen *et al.*, Nat. Commun. **8**, 15376 (2017).

[19] G. Jacob, K. Groot-Berning, S. Wolf, S. Ulm, L. Couturier, S. T. Dawkins, U. G. Poschinger, F. Schmidt-Kaler, and K. Singer, Phys. Rev. Lett. **117**, 043001 (2016).

[20] See Supplemental Material at http://link.aps.org/supplemental/10.1103/PhysRevLett.123.106802 for (i) Methods of praseodymium loading into, detection and extraction from the Paul trap, (ii) experimental setup for single praseodymium ion detection, (iii) annealing procedure after implantation, (iv) data on collected fluorescence signal on the measured spots, and (v) error estimation of precision.

[21] J. B. Wübbena, S. Amairi, O. Mandel, and P. O. Schmidt, Phys. Rev. A **85**, 043412 (2012).

[22] J. F. Ziegler, M. D. Ziegler, and J. P. Biersack, Nucl. Instrum. Methods Phys. Res., Sect. B **268**, 1818 (2010).

[23] S. K. Gayen, B. Q. Xie, and Y. M. Cheung, Phys. Rev. B **45**, 20 (1992).

[24] J. B. Gruber, M. E. Hills, R. M. Macfarlane, C. A. Morrison, and G. A. Turner, Chem. Phys. **134**, 241 (1989).
[25] M. Weber, Solid State Commun. **12**, 741 (1973).
[26] J. Dillon Jr. and L. R. Walker, Phys. Rev. **124**, 1401 (1961).
[27] J. Van der Ziel, M. Sturge, and L. Van Uitert, Phys. Rev. Lett. **27**, 508 (1971).
[28] D. Cherniak, Phys. Chem. Miner. **26**, 156 (1998).
[29] J. Perczel, J. Borregaard, D. E. Chang, H. Pichler, S. F. Yelin, P. Zoller, and M. D. Lukin, Phys. Rev. Lett. **119**, 023603 (2017).
[30] P. Haikka, Y. Kubo, A. Bienfait, P. Bertet, and K. Mølmer, Phys. Rev. A **95**, 022306 (2017).
[31] B. E. Kane, Nature (London) **393**, 133 (1998).
[32] G. Tosi, F. A. Mohiyaddin, V. Schmitt, S. Tenberg, R. Rahman, G. Klimeck, and A. Morello, Nat. Commun. **8**, 450 (2017).
[33] R. Kolesov, S. Lasse, C. Rothfuchs, A. D. Wieck, K. Xia, T. Kornher, and J. Wrachtrup, Phys. Rev. Lett. **120**, 033903 (2018).